

Density changes in amorphous silicon induced by swift heavy ionsSjoerd Roorda ,* Stéphanie Codsi , and Amélie Lacroix *Département de physique, Université de Montréal, 1375 Avenue Thérèse-Lavoie-Roux, Montréal (Québec), H2V 0B3 Canada*Gabrielle G. Long *X-Ray Science Division, Argonne National Laboratory, Argonne, Illinois 60439, USA*Fan Zhang *Material Measurement Laboratory, National Institute of Standards and Technology, Gaithersburg, Maryland 20899, USA*

Steven J. Weigand

*DuPont-Northwestern-Dow Collaborative Access Team Synchrotron Research Center, Northwestern University, Argonne National Laboratory, Argonne, Illinois 60439, USA*Christina Trautmann *GSI Helmholtzzentrum, Materials Research, Planckstrasse 1, 64291 Darmstadt, Germany and Technical University of Darmstadt, 64289 Darmstadt, Germany*

(Received 7 February 2022; revised 13 April 2022; accepted 19 September 2022; published 4 October 2022)

Pure and gold-doped amorphous silicon membranes were irradiated with swift heavy ions (75 MeV Ag or 1.1 GeV Au ions) and studied using small-angle x-ray scattering. The samples that were irradiated with 1.1 GeV Au ions produced a scattering pattern consistent with core-shell-type ion tracks of 2.0 ± 0.1 nm (core) and 7.0 ± 0.3 nm (total) radius irrespective of gold doping, consistent with radii previously observed [9]. The density in the core is nearly 4% different from that of the surrounding material. The entire track (core + shell) is slightly less dense than the surrounding material, yielding an expansion or hammering constant A of 0.036 ± 0.003 nm² per ion track, consistent with the macroscopic “hammering” deformation. No tracks were found in samples irradiated with 75 MeV Ag ions, and no signature specific to the gold impurity doping could be observed.

DOI: [10.1103/PhysRevB.106.144101](https://doi.org/10.1103/PhysRevB.106.144101)**I. INTRODUCTION: ION TRACKS**

The irradiation of materials with swift heavy ions can lead to effects such as macroscopic deformation (lateral growth) [1], mass transport [2], nanoparticle reshaping [3,4], and ion track formation [5]. Ion tracks can commonly be observed in insulators but are rare in metals and semiconductors [6]. Ion tracks can take the form of a long narrow cylinder consisting of a core surrounded by a cylindrical shell, with core and shell radii ranging from less than 1 to 20 nm [6]. The core is considered less dense than the matrix, and the shell is a strained, overdense region surrounding the core. The lower density in the core is inferred from the softness seen in “hollows” by atomic force microscopy of ion tracks in mica [7] and has been directly observed in plan view transmission electron microscopy of tracks in amorphous Si₃N₄ [8]. One of the few (if not the only) materials in which an inverted contrast (i.e., a high density core surrounded by a low density shell) is reported is amorphous silicon (*a*-Si) [9], even though in a very similar material (amorphous germanium) the regular contrast was reported [10].

Understanding track formation in *a*-Si is made more difficult by the curious behavior of silicon. In crystalline silicon (*c*-Si), even 3.4 GeV Kr ions do not leave ion tracks [11]; liquid silicon (*l*-Si) is more dense than both the crystalline and amorphous solid types, but anisotropic deformation [12] and mass transport [13] imply track expansion, and a low-density liquid phase of silicon has been invoked to explain such plastic deformation of *a*-Si under irradiation with swift heavy ions [14].

Theory and modeling have provided significant insight into the mechanism of swift heavy ion track formation, and the most widely accepted scenario is that of a thermal spike [15], in which the energy deposited by the decelerating ion into the electronic system is so rapidly transferred to thermal atomic motion that most of the process can be viewed as a purely thermal phenomenon even though early in the process, essentially all bonds are broken. Other effects such as Coulomb heating (mutual ionic repulsion near the center of the ion track because the target atoms have been temporarily ionized) have not been completely ruled out [16,17]. Because the deposition of energy density (stopping power) is so high and localized (more than 1 keV/nm), the thermal spike model predicts that in some materials melting and even evaporation can occur [18]. Since *l*-Si has a higher density than solid silicon, three

*sjoerd.roorda@umontreal.ca

possible stopping power thresholds might exist: the energy deposition required to melt, the energy required to melt and also reach the temperature where the liquid has expanded to achieve a density lower than the surrounding solid, and, finally, the energy deposition required to melt and evaporate (boil) the core.

Recent measurements on ion tracks in amorphous silicon oxide and amorphous silicon nitride confirmed the normal density changes, exceeding 8% for expansion of the core and 2% for compaction in the shell [19,20]. This raises the question of what the density distribution would be for ion tracks in pure *a*-Si: The amorphous phase of silicon is always less dense than the crystalline phase, and the density deficit can be as little as 1.8 ± 0.1 at.% for *a*-Si made by self-ion implantation [21]. After thermal annealing at 500 °C the density remains virtually unchanged, even if at intermediate temperatures a 0.1% expansion and subsequent compaction take place [22].

In this work, we measure the absolute density of ion tracks in *a*-Si, and we establish a threshold in stopping power required for track formation which is higher than that for some other swift heavy ion track effects. We argue that the ion track is less dense in the core, not more dense as concluded from molecular dynamics simulations [9]. The overall density of the track (core + shell) is lower than that of the *a*-Si matrix, corresponding to a positive hammering constant consistent with the anisotropic deformation seen when multiple ion tracks overlap [12–14].

II. SAMPLE PREPARATION AND CHARACTERIZATION

Amorphous silicon samples were prepared by self-ion implantation into crystalline silicon. Silicon membranes, nominally 2 μm thick, were held at liquid nitrogen temperature and self-implanted on both sides with 0.5, 2, 4, and 5 MeV Si ions to a fluence of 5×10^{15} ions/cm² at each energy. Some samples were also implanted (on both sides) with gold ions to achieve low and high doping levels of 0.005 and 0.125 at.%. An approximately uniform gold concentration profile was aimed for by using a range of energies (0.3, 0.8, 1.5, 2.4, 3.6, 5.1, and 7 MeV) and fluences (ranging from 1.2×10^{13} to 2×10^{15} ions/cm²). The gold concentration was verified by Rutherford backscattering spectrometry and x-ray fluorescence. The intentional contamination with gold was done in an effort to observe segregation, which would indicate a moving liquid-solid interface at some time during the ion track formation process, but no such segregation could be seen.

The thickness of the amorphous membranes, essential information required for the absolute track density measurement, was verified by Fourier transform infrared spectroscopy in transmission, using the known index of refraction of *a*-Si [23,24]. The thickness of individual membranes was found to vary somewhat from sample to sample, between 1950 ± 20 and 2092 ± 4 nm.

In order to make swift heavy ion tracks, samples were irradiated at 1.1 GeV with 1×10^{11} gold ions/cm² or at 75 MeV with 1×10^{10} silver ions/cm². The stopping power of these swift heavy ions in crystalline silicon, according to Stopping and Range of Ions in Matter 2013 (SRIM) [25], amounts

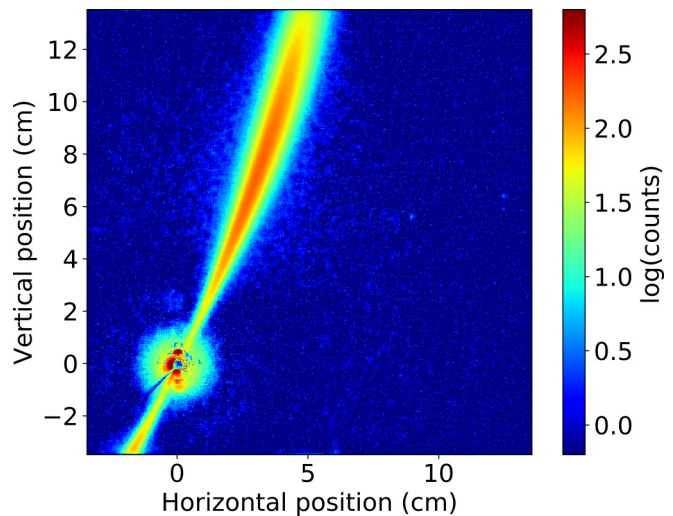


FIG. 1. SAXS image of 1.1 GeV Au ion tracks in (0.005 at.%) gold-doped *a*-Si. An image of an unirradiated *a*-Si membrane of similar thickness was acquired under identical conditions and subtracted. This image was acquired at a nominal tilt angle of 0°; however, the ion tracks are tilted 4.7° away from the surface normal of the membrane, and therefore, the image shows streaks characteristic of tilted cylinders.

to 21.6 and 9.5 keV/nm, respectively. Some of the membranes were not irradiated with swift heavy ions so that they could serve as a reference. Since *a*-Si is similarly bonded but slightly less dense [21] than crystalline silicon, these stopping power values should be slightly reduced (by 1.8%, to 21.2 and 9.3 keV/nm, respectively). The projected range for the swift heavy ions used in this experiment is 13 μm for 75 MeV Ag and 65 μm for Au ions, much more than the membrane thickness of 2 μm .

Small-angle x-ray scattering (SAXS) and medium-angle x-ray scattering from our samples were measured at the Advanced Photon Source (APS) in vacuum with 11.4 keV x rays in transmission geometry with detectors placed at 8502 and 1017 mm; the angle between incident x rays and sample normal was set at nominal values of -20° , 0° , 8° , and 45° . For a detailed description of the SAXS instrumentation, see Ref. [26]. The x-ray scattering intensity data were corrected for the detector dark field, sample absorption, and the x-ray polarization factor and were placed on an absolute scale by means of comparison with a glassy-carbon secondary standard [27].

III. RESULTS

An example of a SAXS image of ion tracks made by 1.1 GeV Au ions incident on 50 ppm Au-doped *a*-Si is shown in Fig. 1. The image from the detector at 8502 mm is shown, where an image from unirradiated (i.e., track free) *a*-Si has been subtracted. For this image, the x rays were incident on the sample at a nearly normal angle, but since the tracks are a few degrees off the surface normal, a streak pattern is observed characteristic of tilted long narrow cylinders. Because we used edge-supported irradiated membranes and subtracted the image from an unirradiated one, the pattern visible in the

image is due to only ion tracks; it does not need to be corrected for absorption, and its intensity is proportional to the areal density of ion tracks in the sample and to the electron density contrast in each track.

Similar streaks were observed in *a*-Si membranes irradiated with 1.1 GeV Au ions, independent of impurity content. By taking images at four different angles, the orientation of the ion tracks within the membranes could be deduced, and the intensity as a function of Q along an axis perpendicular to the symmetry axis could be extracted. This intensity can be described by a sum of Bessel functions [28,29]; an arbitrary radial profile can be described as a series of concentric cylindrical shells of, within each shell, constant electron density. We used a density profile consisting of a core with low density (compared to the matrix) surrounded by a slightly compacted shell, with smooth error function transitions between the density of the core and shell and between shell and the surrounding matrix:

$$\rho(r) = \rho_c \frac{[\operatorname{erf}(\frac{r-R_c}{w_c}) - 1]}{2} + \rho_s \frac{[1 - \operatorname{erf}(\frac{r-R_s}{w_s})]}{2} \quad (1)$$

where $\rho(r)$ is the density difference from the *a*-Si matrix at distance r from the track center and ρ_c , ρ_s , R_c , R_s , w_c , and w_s are the core and shell maximum density differences, radii, and transition widths, respectively. We used 200 concentric shells of 0.75 Å thickness to create a smooth profile, and the widths of the transition regions were 2.5 and 0.8 nm; varying these widths only slightly improved the quality of the fits without significantly affecting the extracted values for radii and densities. The form factor is then calculated using an expression similar to Eq. (9) from Ref. [29], generalized to N concentric shells R_i and with J_1 being the Bessel function of the first kind:

$$F(q, \rho) \sim \sum_{i=1}^N 2\rho(R_i) \left(\frac{R_i}{q} J_1(qR_i) - \frac{R_{i-1}}{q} J_1(qR_{i-1}) \right) \quad (2)$$

Naively, the relative densities of the core and shell would be governed by the requirement that the total number of atoms within the outermost track radius be conserved, and if that occurs, the shell density would be determined by the core density and the ratio of the core and shell radii. However, the best fits were obtained by making the shell density an additional fitting parameter. This core-shell structure is similar to the one used by [9,19] to fit their data, except that in our case the absolute scattering intensity is known so that from the fits combined with the number of ion tracks per unit surface area, the electron density in the core and shell could be determined.

Example fits are shown in Fig. 2. The solid red line shows the best fit, obtained after releasing the constraint that mass per unit volume be conserved. The best fit is much better than the dashed blue line, which is the best fit that could be obtained with mass conservation, in which any atoms missing from (or added to) the core must be added to (or taken from) the shell, with an unchanged total volume. The inset shows the radial density profiles deduced from the fits, in percent deviation from the *a*-Si density, assuming a low-density core and a compressed shell and showing the smooth core-shell and shell-matrix transitions. Similar fits were performed for the streaks seen in the same sample but at different incident

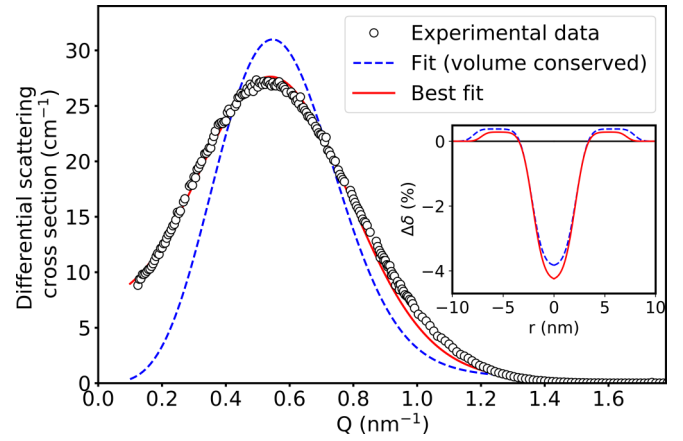


FIG. 2. Experimental data and fit for the streak shown in Fig. 1, normalized and expressed as the differential scattering cross section (in cm^{-1}) as a function of scattering vector (in nm^{-1}). Black open circles: Experimental data constructed using image data from both detectors. Blue dashed line: Fit with imposed volume conservation; density change in core exactly balanced by that in the shell. Red solid line: Best fit without overall density conservation. The inset shows the ion track density profile deduced from the fits in atomic percent deviation from the *a*-Si density as a function of distance from the center. Dashed blue and solid red lines are as in the main panel.

angles and for the other (pure and higher Au concentration) samples. The core and total radii from all fits are reported in Table I. Because the ion tracks in this study extended over the entire (known) thickness of the irradiated membranes, the differential scattering cross section and therefore [30] the absolute densities of the core-shell structure in *a*-Si could also be determined; these values are shown in Fig. 3 and are also reported in Table I.

We have also considered density profiles that have an additional feature, namely, a narrow spike of increased density near the cylinder axis, representing the segregated gold impurities. The differences between $I(Q)$ intensities calculated with and without such a spike are negligibly small compared to the noise in the data.

The SAXS images of samples irradiated with 75 MeV Ag ions showed no signal attributable to ion tracks, either in normal incidence or when the samples were tilted with respect to the incident x rays. We also inspected images taken on these samples with cameras at 1017 and 200 mm (low- and wide-angle ranges), but no signature signal of tilted cylindrical structures could be seen in any image. We also evaluated samples with slightly lower ion energy (70 MeV), higher dose (3×10^{10} ions/ cm^2), and geometry (*a*-Si on a substrate or edge-supported membranes) but failed to find any trace of ion tracks in these samples. Therefore, we must conclude that irradiation of *a*-Si with swift heavy ions with a stopping power of 9.5 keV/nm or less does not leave tracks observable in SAXS.

Figure 3 shows the core and shell densities for each of the samples and at each x-ray incident angle, compared to the absolute densities of *c*- and *a*-Si. Since SAXS determines only the numerical value of the density contrast but not its sign, there are two possibilities: (1) a high-density core, shown by solid symbols and solid lines, and low-density shell (not

TABLE I. Ion track properties deduced from the best fits to the SAXS data; the density is expressed as a percentage change relative to *a*-Si density. Uncertainties in radii are only due to fitting; uncertainties in densities include the error in areal track density (ion fluence). Errors in the mean are standard deviations.

Sample	R_{core} (nm)	R_{total} (nm)	Core density (%)	Shell density (%)
Pure <i>a</i> -Si	2.01 ± 0.04	7.24 ± 0.16	-3.3 ± 0.4	0.26 ± 0.03
Low gold doped <i>a</i> -Si	2.04 ± 0.08	7.02 ± 0.18	-4.1 ± 0.5	0.35 ± 0.04
High gold doped <i>a</i> -Si	1.95 ± 0.06	6.69 ± 0.18	-4.5 ± 0.5	0.39 ± 0.04
Mean	2.0 ± 0.1	7.0 ± 0.3	-4.0 ± 0.7	0.33 ± 0.08

shown; as argued by Bierschenk *et al.* [9]) and (2) a low-density core, shown by open symbols and solid lines, and high-density shell, shown by open symbols and dashed lines. The horizontal black line shows the atomic density of *c*-Si, and the gray band shows the range of densities observed in *a*-Si made by ion implantation and thermal annealing. The question regarding a high- or low-density core will be discussed in the next section, but a few items can be noted first: The density of the core and shell should, of course, be independent of measurement angle, and this is, indeed, the case except for two of the data points at near-normal incidence. In that case the relative error in the tilt angle between x rays and the ion track is the largest; therefore, it is not surprising that the largest variations occur at a 0° nominal tilt angle. There also appears to be a small gold doping effect, with slightly larger density changes provoked when gold doping is present. However, the change is small compared to the 10% sample-to-sample uniformity in terms of irradiation dose with swift heavy ions, and a firm conclusion about the doping effect would require confirmation.

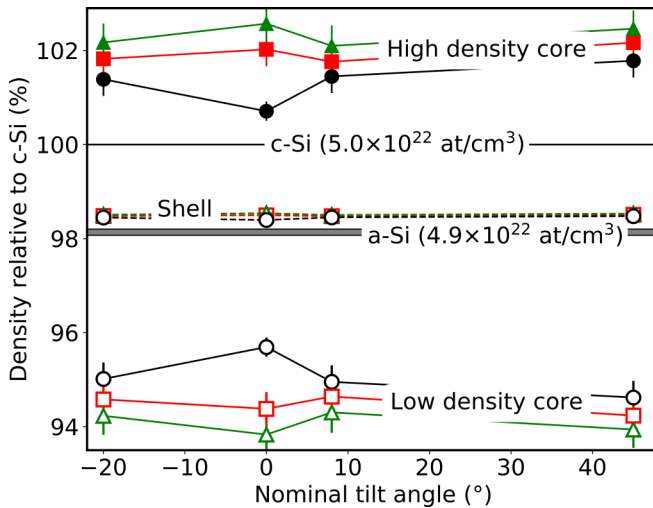


FIG. 3. Atomic densities of the core and shell for all samples and all measurement angles. The black horizontal line at 100% corresponds to the density of *c*-Si, and the gray band near 98% corresponds to *a*-Si made by ion implantation. Open symbols correspond to the low-density core/high-density shell ansatz, and solid symbols correspond to the high-density core/low-density shell ansatz (shell densities in that case are not shown and fall slightly below 98%). Circles, squares, and triangles correspond to pure, low, and high Au-doped *a*-Si, respectively. Error bars correspond to 1σ values in the χ^2 optimization.

IV. DISCUSSION

A. Density contrast: Expanded or compacted core?

While the SAXS measurement cannot distinguish between a positive and negative contrast, in other words between an overdense core with an underdense shell and an underdense core with a compacted shell, the density profile of the single ion track must be consistent with the macroscopic effects seen when multiple tracks overlap, such as *a*-Si anisotropic deformation [12] and *a*-Si mass transport [13,14]. From the absolute values of radii and densities reported in Table I, we can compare the total track radius with the radius of a cylinder containing the same number of atoms with the original *a*-Si density and determine the net expansion in terms of a surface gain (in a plane perpendicular to the track axis); this amounts to $0.036 \pm 0.003 \text{ nm}^2$. This gain corresponds to a positive hammering constant A , for which values have been reported over a range of stopping powers.

Figure 4 reproduces those values for the hammering constant as open symbols and in addition shows, as a red circle, the hammering constant for a single ion track deduced from our data. Clearly, the single-track expansion agrees well, both qualitatively and quantitatively, with the macroscopic deformation observed earlier. Since Bierschenk *et al.* [9] did not report absolute values for the core and shell densities, one cannot calculate a hammering constant from their data; however,

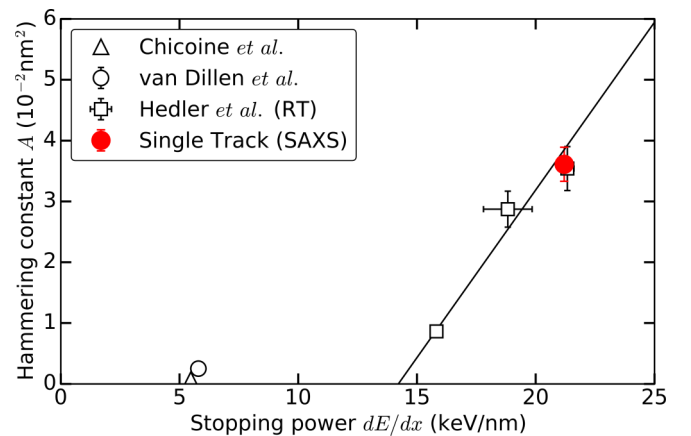


FIG. 4. Hammering constant versus stopping power as reported from anisotropic deformation (triangle, Ref. [12]) and mass transport (open circle, Ref. [13], and open squares, Ref. [14]) compared to that for a single ion track as deduced from our SAXS measurements (solid red circle). The straight line is taken from Ref. [14] and refers to room-temperature irradiation.

the hammering constant deduced for a compacted-core track must be negative, which is clearly in qualitative disagreement with the experimental data from macroscopic deformation, although there is one caveat: The stopping powers used in Ref. [9], 10.6 and 15.6 keV/nm, fall just below the lowest stopping power of 15.8 keV/nm used in Ref. [14] and well above that of 6 keV/nm used in Ref. [12]. It cannot be ruled out that the hammering constant changes from positive to negative between 6 and 10 keV/nm and then back from negative to positive between 15.6 and 15.8 keV/nm.

The scenario for track formation resulting in a low-density core and compacted shell is therefore along the following lines: A narrow cylinder melts and expands (either by thermal expansion of metallic ℓ -Si or by passing directly to a low-density liquid phase as proposed in Ref. [14]), and the expanding cylinder compresses and compacts a cold and solid region around it, the shell. When the center cools down, there is now slightly more space to fill than before, and the core ends up with a somewhat reduced density. This scenario is strongly supported by the recent report of significant asymmetry in the elastic properties of a -Si when comparing tension and compression [31]. Namely, under tension a -Si remains fully elastic until catastrophic failure, but under compaction, when the stress exceeds 4.5 GPa, a -Si deforms through flow and irreversibly compacts, exactly the behavior required for a compacted shell, implying that the stopping power threshold for permanent track formation corresponds to the situation where the stress caused by the expanding core exceeds the yield strength of a -Si under compression. Conversely, the asymmetry leaves no pathway for an underdense shell caused by core compaction because under tension the shell either behaves fully elastically or physically separates from the compacted core.

In Ref. [9], the argument for an overdense core was deduced solely from molecular dynamics simulations of the track immediately after the energy deposition. These simulations used the Tersoff potential [32], but while this potential was, indeed, optimized to describe both liquid and solid silicon, it may not be optimal for the simulation of ion track formation. Namely, the simulated melting temperature of about 3000 K is nearly twice as high as the experimental one [33]. Moreover, the simulated melting is accompanied by a compaction (ℓ -Si is, indeed, denser than solid Si); however, real ℓ -Si undergoes thermal expansion [34] larger than that of c -Si [35] when heated from its real melting temperature to 3000 K to the extent that it is now less dense than solid Si (crossover temperatures near 2770 and 2920 K for c -Si and a -Si, respectively). Consequently, the density of ℓ -Si just above 3000 K is considerably overestimated in simulations using the Tersoff potential. Indeed, recent density functional theory calculations found a track core either more or less dense than its surroundings depending on the stopping power [36].

B. Stopping power considerations

We now compare our data for track radii to the results obtained by Bierschenk *et al.* [9] using 89 and 185 MeV gold ions, as shown as a function of stopping power in Fig. 5. The comparison should be made with the as-implanted data since our a -Si membranes were not annealed. The condi-

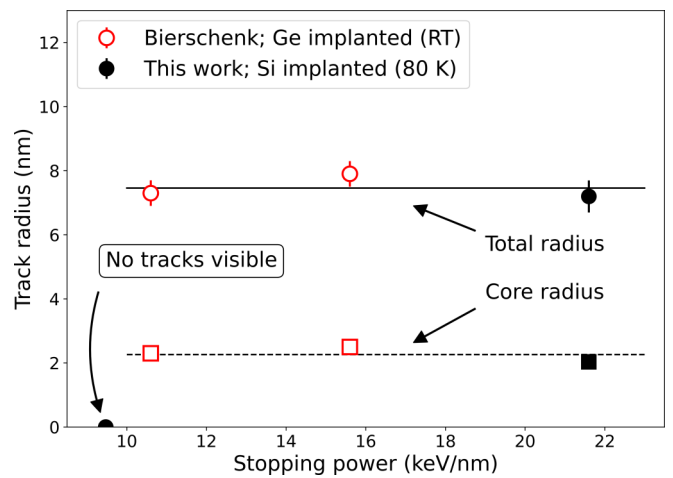


FIG. 5. Track radii deduced from SAXS as a function of stopping power. Open red symbols: After Ref. [9]. Solid black symbols: This work. Solid and dashed lines indicate mean values of nonzero data points.

tions for the preparation of a -Si were slightly different: We used self-irradiation at 80 K, whereas Bierschenk *et al.* used room-temperature Ge ion implantation. In view of the significant difference between track radii in as-implanted and annealed a -Si [9], some adjustment factor should, perhaps, be applied when comparing track radii. In addition, there are a few minor differences in the track fitting procedure we used compared to that employed by Bierschenk *et al.*: We used a smoothly varying density profile and did not include the transition region in the total track radius, whereas Bierschenk *et al.* used a box profile and a Gaussian broadening to account for interface roughness and track-to-track variations. Because of the smooth transition region we employed, the density profile extends beyond the nominal value of the total track radius. Nevertheless, our datum seems to confirm that both the core and total radius appear to be largely independent of the stopping power, and the lack of variation in track radii with stopping power is quite surprising, although a similar very weak dependence on stopping power was reported in Si_3N_4 [37,38]. Since the hammering constant does exhibit a strong linear dependence on stopping power (see Fig. 4), the weak dependence for the track radii implies that the core density should vary with stopping power.

For a stopping power somewhere between 9.5 and 10.6 keV/nm a sudden threshold appears, and below it, the linear dependence between the stopping power and track radius is no longer valid, and no tracks are visible in SAXS. The absence of visible ion tracks for ions with a stopping power of 9.5 keV/nm is puzzling because at even lower stopping powers, phenomena associated with swift heavy ion irradiation have been observed, namely, macroscopic deformation at 5.8 keV/nm [12] and macroscopic transport at 5.5 keV/nm [13].

Conceptually, one can identify multiple thresholds involved in ion track formation in a -Si: the stopping power where the material melts, the stopping power where the metallic liquid (initially more dense than the solid) becomes less dense than the surrounding matrix, the stopping power where

thermal expansion creates a stress exceeding the *a*-Si yield strength, and the stopping power where the liquid boils. Indeed, the experimental data show at least one hard threshold (near 9.5 keV/nm for permanent track formation visible in SAXS) as well as a clear discontinuity (near 14 keV/nm; see Fig. 4). The temperatures required for each threshold would be $T = 1200$ °C (melting of *a*-Si), 2700 °C–2900 °C (where, through thermal expansion, the *l*-Si density becomes equal to that of *a*-Si), and 3265 °C (boiling of *l*-Si). To estimate the liquid-solid density crossover, we used for *a*-Si its room-temperature atomic density [21] and a thermal expansion coefficient that is 6.5% less [22] than that of *c*-Si [39,40]. For liquid silicon, we linearly extrapolated the recommended values [34,35].

The heat of melting of *a*-Si is 50.55 (latent heat of *c*-Si) + 13.7 (heat of crystallization of *a*-Si) kJ/mol, or 0.67 eV/atom, and the heat of evaporation of Si is nearly 4 eV/atom. The heat capacity changes somewhat over the temperature of interest, but for a rough estimate we can use a constant value of 0.7 J/gK. Thus, the energies required to respectively melt, melt and heat to equal densities, and melt and boil a 1 nm section of a 2 nm radius *a*-Si cylinder would be 0.56, 0.76, and 3.3 keV. Assuming that only 33% of the energy deposited by the ion effectively heats the ion track (the rest being carried away by energetic electrons or thermal diffusion), this would correspond to stopping power thresholds of 1.7 keV/nm (for only melting), 2.3 keV/nm (to reach equal densities between hot *l*-Si and *a*-Si), and 9.9 keV/nm (for melting and evaporation or exceeding the yield strength). If the observed threshold for track formation (between 9.5 and 10.5 keV/nm) corresponded to only melting, 95% of the deposited energy would have to be lost to the track surroundings. Thus, the conclusion that there are two or three thresholds involving melting, melting and thermal expansion, and thermal expansion exceeding yield strength seems reasonable.

V. CONCLUSIONS

In conclusion, we have used SAXS to study ion tracks in pure and gold-doped amorphous silicon membranes. Irradia-

tion with 1.1 GeV Au ions (21.6 keV/nm stopping power) resulted in core-shell ion tracks with a core and total diameter of 2.0 ± 0.1 and 7.0 ± 0.3 nm, respectively, irrespective of gold doping and in line with earlier measurements. No ion tracks were visible after irradiation with 75 MeV Ag ions (stopping power of 9.5 keV/nm). This suggests that two thresholds exist, one corresponding to the onset of macroscopic deformation and another, at a higher stopping power, required for formation of tracks visible in SAXS. The density change in the 2 nm core is $4.0\% \pm 0.7\%$ less dense than the original material. The surrounding shell is slightly compacted (by $0.33\% \pm 0.08\%$) but not enough to completely counteract the core expansion. The overall ion track is therefore slightly expanded, which leads to a hammering constant of 0.036 ± 0.003 nm² for a single ion track, qualitatively and quantitatively in excellent agreement with the hammering deformation.

ACKNOWLEDGMENTS

This work was supported by the Fonds de recherche - Nature et technologies (FRQNT) and the Natural Sciences and Engineering Research Council (NSERC). S.R. acknowledges L. Godbout for assistance with the operation of the MV Tandem accelerator, and S.C. acknowledges J. Codsì for his help and input. The results presented here are based on a UMAT experiment, which was performed at the X0 beamline of the UNILAC at the GSI Helmholtzzentrum für Schwerionenforschung, Darmstadt (Germany), in the frame of FAIR Phase-0. This work was performed at the DuPont-Northwestern-Dow Collaborative Access Team (DND-CAT) located at Sector 5 of the Advanced Photon Source (APS). DND-CAT is supported by Northwestern University, the Dow Chemical Company, and DuPont de Nemours, Inc. This research used resources of the Advanced Photon Source, a U.S. Department of Energy (DOE) Office of Science User Facility operated for the DOE Office of Science by Argonne National Laboratory under Contract No. DE-AC02-06CH11357. The authors gratefully acknowledge an anonymous referee for bringing a recent paper (Ref. [31]) to their attention.

-
- [1] S. Klaumünzer and G. Schumacher, Dramatic Growth of Glassy Pd₈₀Si₂₀ During Heavy-Ion Irradiation, *Phys. Rev. Lett.* **51**, 1987 (1983).
 - [2] L. Cliche, S. Roorda, M. Chicoine, and R. A. Masut, Directional Mass Transport by Momentum Transfer from Ion Beam to Solid, *Phys. Rev. Lett.* **75**, 2348 (1995).
 - [3] E. A. Dawi, A. M. Vredenberg, G. Rizza, and M. Toulemonde, Ion-induced elongation of gold nanoparticles in silica by irradiation with Ag and Cu swift heavy ions: Track radius and energy loss threshold, *Nanotechnology* **22**, 215607 (2011).
 - [4] S. Roorda, T. van Dillen, A. Polman, C. Graf, A. van Blaaderen, and B. J. Kooi, Aligned gold nanorods in silica made by ion irradiation of core-shell colloidal particles, *Adv. Mater.* **16**, 235 (2004).
 - [5] R. L. Fleischer, P. B. Price, and R. M. Walker, Tracks of charged particles in solids, *Science* **149**, 383 (1965).
 - [6] M. Toulemonde, S. Bouffard, and F. Studer, Swift heavy ions in insulating and conducting oxides: Tracks and physical properties, *Nucl. Instrum. Methods Phys. Res. Sect. B* **91**, 108 (1994).
 - [7] F. Thibaudau, J. Cousty, E. Balanzat, and S. Bouffard, Atomic-Force-Microscopy Observations of Tracks Induced by Swift Kr Ions in Mica, *Phys. Rev. Lett.* **67**, 1582 (1991).
 - [8] K. Nakajima, Y. Morita, M. Suzuki, K. Narumi, Y. Saitoh, N. Ishikawa, K. Hojou, M. Tsujimoto, S. Isoda, and K. Kimura, Direct observation of fine structure in ion tracks in amorphous Si₃N₄ by TEM, *Nucl. Instrum. Methods Phys. Res. Sect. B* **291**, 12 (2012).
 - [9] T. Bierschenk, R. Giulian, B. Afra, M. D. Rodriguez, D. Schauries, S. Mudie, O. H. Pakarinen, F. Djurabekova, K. Nordlund, O. Osmani, N. Medvedev, B. Rethfeld, M. C. Ridgway, and P. Kluth, Latent ion tracks in amorphous silicon, *Phys. Rev. B* **88**, 174111 (2013).

- [10] M. C. Ridgway, T. Bierschenk, R. Giulian, B. Afra, M. D. Rodriguez, L. L. Araújo, A. P. Byrne, N. Kirby, O. H. Pakarinen, F. Djurabekova, K. Nordlund, M. Schleberger, O. Osmani, N. Medvedev, B. Rethfeld, and P. Kluth, Tracks and Voids in Amorphous Ge Induced by Swift Heavy-Ion Irradiation, *Phys. Rev. Lett.* **110**, 245502 (2013).
- [11] M. Toulemonde, J. Dural, G. Nouet, P. Mary, J. F. Hamet, M. F. Beaufort, J. C. Desoyer, C. Blanchard, and J. Auleytner, High energy heavy ion irradiation of silicon, *Phys. Status Solidi A* **114**, 467 (1989).
- [12] T. van Dillen, M. J. A. De Dood, J. J. Penninkhof, A. Polman, S. Roorda, and A. M. Vredenberg, Ion beam-induced anisotropic plastic deformation of silicon microstructures, *Appl. Phys. Lett.* **84**, 3591 (2004).
- [13] M. Chicoine, S. Roorda, L. Cliche, and R. A. Masut, Directional effects during ion implantation: Lateral mass transport and anisotropic growth, *Phys. Rev. B* **56**, 1551 (1997).
- [14] A. Hedler, S. L. Klaumünzer, and W. Wesch, Amorphous silicon exhibits a glass transition, *Nat. Mater.* **3**, 804 (2004).
- [15] M. Toulemonde, E. Paumier, and C. Dufour, Thermal spike model in the electronic stopping power regime, *Radiat. Eff. Defects Solids* **126**, 201 (1993).
- [16] E. M. Bringa and R. E. Johnson, Coulomb Explosion and Thermal Spikes, *Phys. Rev. Lett.* **88**, 165501 (2002).
- [17] P. Baril, L. J. Lewis, and S. Roorda, A numerical study of energy transfer mechanisms in materials following irradiation by swift heavy ions, *Eur. Phys. J. B* **71**, 27 (2009).
- [18] M. Toulemonde, C. Dufour, and E. Paumier, Transient thermal process after a high-energy heavy-ion irradiation of amorphous metals and semiconductors, *Phys. Rev. B* **46**, 14362 (1992).
- [19] P. Mota-Santiago, H. Vazquez, T. Bierschenk, F. Kremer, A. Nadzri, D. Schauries, F. Djurabekova, K. Nordlund, C. Trautmann, S. Mudie, M. C. Ridgway, and P. Kluth, Nanoscale density variations induced by high energy heavy ions in amorphous silicon nitride and silicon dioxide, *Nanotechnology* **29**, 144004 (2018).
- [20] P. Kluth, C. S. Schnorr, O. H. Pakarinen, F. Djurabekova, D. J. Sprouster, R. Giulian, M. C. Ridgway, A. P. Byrne, C. Trautmann, D. J. Cookson, K. Nordlund, and M. Toulemonde, Fine Structure in Swift Heavy Ion Tracks in Amorphous SiO₂, *Phys. Rev. Lett.* **101**, 175503 (2008).
- [21] J. S. Custer, M. O. Thompson, D. C. Jacobson, J. M. Poate, S. Roorda, W. C. Sinke, and F. Spaepen, Density of amorphous Si, *Appl. Phys. Lett.* **64**, 437 (1994).
- [22] C. A. Volkert, Density changes and viscous flow during structural relaxation of amorphous silicon, *J. Appl. Phys.* **74**, 7107 (1993).
- [23] M. J. A. De Dood, A. Polman, T. Zijlstra, and E. W. J. M. Van der Drift, Amorphous silicon waveguides for microphotonics, *J. Appl. Phys.* **92**, 649 (2002).
- [24] J. E. Fredrickson, C. N. Waddell, W. G. Spitzer, and G. K. Hubler, Effects of thermal annealing on the refractive index of amorphous silicon produced by ion implantation, *Appl. Phys. Lett.* **40**, 172 (1982).
- [25] J. F. Ziegler, M. D. Ziegler, and J. P. Biersack, Srim—The stopping and range of ions in matter (2010), *Nucl. Instrum. Methods Phys. Res. Sect. B* **268**, 1818 (2010).
- [26] S. J. Weigand and D. T. Keane, DND-CAT's new triple area detector system for simultaneous data collection at multiple length scales, *Nucl. Instrum. Methods Phys. Res. Sect. A* **649**, 61 (2011).
- [27] F. Zhang, J. Ilavsky, G. G. Long, J. P. G. Quintana, A. J. Allen, and P. R. Jemian, Glassy carbon as an absolute intensity calibration standard for small-angle scattering, *Metall. Mater. Trans. A* **41**, 1151 (2010).
- [28] P. Mittelbach and G. Porod, Zur Röntgenkleinwinkelstreuung verdünnter kolloider Systeme, *Acta Phys. Austriaca* **14**, 185 (1961).
- [29] M. Engel, B. Stühn, J. J. Schneider, T. Cornelius, and M. Naumann, Small-angle x-ray scattering (SAXS) off parallel, cylindrical, well-defined nanopores: From random pore distribution to highly ordered samples, *Appl. Phys. A* **97**, 99 (2009).
- [30] A. Guinier, *X-Ray Diffraction in Crystals, Imperfect Crystals, and Amorphous Bodies* (Freeman, New York, 1963).
- [31] Y. Wang, J. Ding, Z. Fan, L. Tian, M. Li, H. Lu, Y. Zhang, E. Ma, J. Li, and Z. Shan, Tension-compression asymmetry in amorphous silicon, *Nat. Mater.* **20**, 1371 (2021).
- [32] J. Tersoff, Empirical interatomic potential for silicon with improved elastic properties, *Phys. Rev. B* **38**, 9902 (1988).
- [33] M. O. Thompson, G. J. Galvin, J. W. Mayer, P. S. Peercy, J. M. Poate, D. C. Jacobson, A. G. Cullis, and N. G. Chew, Melting Temperature and Explosive Crystallization of Amorphous Silicon during Pulsed Laser Irradiation, *Phys. Rev. Lett.* **52**, 2360 (1984).
- [34] Y. S. Touloukian, R. K. Kirby, E. R. Taylor, and T. Y. R. Lee, *Thermophysical Properties of Matter: The TPRC Data Series, Thermal Expansion-Nonmetallic Solids* (Plenum Publishing, New York, 1977), Vol. 13.
- [35] M. J. Assael, I. J. Armyra, J. Brillo, S. V. Stankus, J. Wu, and W. A. Wakeham, Reference data for the density and viscosity of liquid cadmium, cobalt, gallium, indium, mercury, silicon, thallium, and zinc, *J. Phys. Chem. Ref. Data* **41**, 033101 (2012).
- [36] G. S. Khara, S. T. Murphy, S. L. Daraszewicz, and D. M. Duffy, The influence of the electronic specific heat on swift heavy ion irradiation simulations of silicon, *J. Phys.: Condens. Matter* **28**, 395201 (2016).
- [37] A. Ibrayeva, A. Mutali, A. Sohatsky, A. Janse van Vuuren, J. O'Connell, and V. Skuratov, High energy heavy ion tracks in nanocrystalline silicon nitride, in *Proceedings of the 14th International Conference "Interaction of Radiation with Solids"* (Minsk, Belarus, 2021), pp. 125–127.
- [38] A. Janse van Vuuren, A. Ibrayeva, V. Skuratov, and M. Zdorovets, The effects of SHIs on Si₃N₄, in *Proceedings of the 29th International Conference on Atomic Collisions in Solids and 11th International Symposium on swift Heavy Ions in Matter* (Helsinki, 2022).
- [39] *Properties of Crystalline Silicon*, edited by R. Hull (INSPEC, London, UK, 1999).
- [40] M. Watanabe, M. Adachi, T. Morishita, K. Higuchi, H. Kobatake, and H. Fukuyama, Does supercooled liquid Si have a density maximum?, *Faraday Discuss.* **136**, 279 (2007).